

Air–Sea Interactions and Biogeochemical Responses to Medicane Daniel

Babita Jangir and Ehud Strobach

Institute of Soil, Water and Environmental Sciences, Volcani Institute, Agriculture Research
Organization, Rishon LeTsiyon, Israel

*Corresponding author: Babita Jangir (bj11@iitbbs.ac.in)

Abstract: Medicane Daniel, formed on 4-12 September 2023, stands out as the deadliest recorded storm in Mediterranean history. In this study, we investigate the role of sea features in the intensification of the medicane Daniel and the response of biogeochemical properties to the storm. Our results show that medicane Daniel intensified immediately prior to landfall in a coastal environment characterized by the co-occurrence of a warm-core eddy (WCE), elevated ocean heat content, and a moderate marine heatwave (MHW), suggesting that sea anomalies may have supported or modulated the intensification under favorable atmospheric forcing. Additionally, observations from the high-resolution Surface Water and Ocean Topography (SWOT) satellite reveal a larger anticyclonic eddy than that depicted in lower-resolution products, thereby further supporting the hypothesis of sea-induced intensification. The favorable conditions at the sea before landfall were accompanied by moisture convergence and moisture supply in the atmosphere above, leading to intense precipitation in this region. Biogeochemical properties were strongly affected by cyclone-induced subsurface vertical mixing and upwelling. Focusing on two eddies in the vicinity of the maximum cyclone intensity, we found that the observed vertical displacement of the deep chlorophyll maximum exceeds that expected by direct wind-driven upwelling alone, suggesting additional contribution from a structural isopycnal adjustment triggered by the neutralization of eddy vorticity. We propose that the medicane destabilizes the eddies' internal balance, leading to a large-scale reorganization of the water column that persists longer in the WCE than the transient response observed in the cold-core eddy (CCE).

Key Words: Medicanes, eddies, marine heatwave, medicane Daniel, SWOT satellite, biogeochemistry

Key Points:

- 33 ● Co-occurring warm-core eddies, marine heatwave, and elevated ocean heat content
34 provided support for the rapid intensification of medicane Daniel near landfall.
- 35 ● High-resolution SWOT observations indicate stronger and larger eddy structures than
36 conventional datasets, supporting their critical role in air–sea interactions.
- 37 ● Interaction with warm-core eddies amplifies vertical mixing and nutrient supply,
38 leading to enhanced chlorophyll and productivity responses.
- 39 ● Cyclone-induced biogeochemical response is influenced by subsurface restructuring
40 and isopycnal adjustment, exceeding expectations from Ekman-driven upwelling alone.
- 41 ● Results demonstrate that compound ocean extremes can significantly enhance both
42 cyclone intensity and ocean biogeochemical impacts.

43

44 **1. Introduction:**

45 The Mediterranean region is recognized as a climate change hotspot (IPCC, 2021), warming at
46 a rate up to 1.5 times faster than the global average (MedECC, 2020; Zittis et al., 2022;
47 Khodayar et al., 2025). Situated between the arid climate of North Africa and the temperate
48 and wet climate of Central Europe, the Mediterranean region is particularly vulnerable to future
49 climate impacts. Surface temperature in this region is projected to continue increasing, but the
50 precipitation tends to decrease (Cherif et al., 2020; Reale et al., 2022). As a consequence, the
51 magnitude of extreme events such as Mediterranean cyclones, marine heatwaves (MHWs), and
52 intense droughts is projected to increase under future climate scenarios (MedECC, 2020;
53 Hochman et al., 2021; Zittis et al., 2022).

54

55 Medicanes are a subcategory of Mediterranean cyclones, which can resemble hurricanes in
56 both intensity and impact. They often bring torrential rainfall, flash floods, powerful winds,
57 storm surges, and hazardous sea conditions. Such events pose significant risks, particularly to
58 coastal communities and urban centers, threatening homes, livelihoods, and natural ecosystems
59 (Hochman et al., 2021; Khodayar et al., 2025). Similar to Mediterranean cyclones, medicane’s
60 intensity is projected to increase under future climate scenarios, but with lower frequency
61 (González-Alemán et al., 2019). Despite their strong impact, the full extent of the damage
62 medicanes inflict, both socially and economically, remains insufficiently understood.

63 Moreover, their potential impact on ocean biogeochemistry is under-researched and often
64 poorly communicated, leaving a critical gap in public awareness and scientific insight.

65

66 Medicanes are also known as ‘tropical-like cyclones’ because they have tropical cyclone-like
67 characteristics such as a cloud-free calm "eye," spiralling cloud bands, and strong winds near
68 the vortex centre. These features may be associated with the absence of fronts, weak vertical
69 wind shear, and a warm-core with an axisymmetric structure (Miglietta et al., 2019; Flaounas
70 et al., 2022; Panegrossi et al., 2023). The formation of cyclones in the Mediterranean region
71 including medicanes, is primarily driven by baroclinic instability and Rossby wave breaking
72 (Raveh-Rubin and Flaounas, 2017; Flaounas et al., 2022). As these systems evolve and reach
73 their mature stage, medicanes can intensify and be sustained through exchanges of heat and
74 momentum at the air-sea interface (Emanuel, 2005). The development of intense
75 Mediterranean cyclones is frequently associated with southward shifts of the polar jet, which
76 enable air masses with high potential vorticity to enter the Mediterranean region, thereby
77 initiating baroclinic instability similar to that observed during extratropical cyclone
78 development over open oceans (Flocas, 2000; Trigo et al., 2002; Nicolaidis et al., 2006; Fita
79 et al., 2007; Claud et al., 2010; Kouroutzoglou et al., 2011; Flaounas et al., 2015). Raveh-Rubin
80 and Flaounas (2017) identified Rossby wave breaking as a frequent precursor to Mediterranean
81 cyclogenesis, while Flaounas et al. (2015) further emphasized that the cyclogenesis
82 environment in the region is characterized by strong horizontal shear, driving these cyclones
83 to follow a typical baroclinic life cycle. Furthermore, Flaounas et al. (2025) also highlight the
84 importance of these atmospheric variables in the genesis and intensification of medicane
85 Daniel. In this manuscript, we primarily focus on potential atmospheric and oceanic precursors
86 that are associated with Daniel’s intensification and ensuing precipitation.

87

88 Furthermore, the role of underlying ocean eddies and MHWs in modulating the deepening of
89 a cyclone is often overlooked. Recent studies have highlighted the critical role of ocean eddies
90 and MHWs in modulating cyclone’s deepening in the Mediterranean region (Jangir et al., 2023,
91 2024; Mishra et al., 2024; Strobach et al., 2024). In particular, Jangir et al. (2024) demonstrated
92 the significant intensification of medicane Ianos due to the presence of a strong MHW, making
93 it the only category 2 cyclone observed in the Mediterranean Sea. In contrast, other medicanes
94 such as Zorbas and Apollo intensified primarily due to the interaction with warm-core eddies
95 (WCEs) along their paths. Mishra et al. (2024) reported that if we remove these Sea Surface
96 Temperature (SST) anomalies from the path of medicane Ianos, the medicane will still form,

97 but with a reduced intensity. Strobach et al. (2024) reported that ocean mesoscale eddies in the
98 Eastern Mediterranean can significantly influence extreme weather, as shown during the heavy
99 rainfall event in Israel that occurred from January 8 to 10, 2020. High-resolution coupled
100 ocean-atmosphere simulations captured the event more accurately than uncoupled ones. The
101 study by Strobach et al. (2024) highlights how eddies can enhance atmospheric moisture and
102 meso-cyclone development, intensifying local extremes.

103

104 As efforts continue to enhance the accuracy of cyclone intensity forecasts, the potential
105 influence of eddies, MHWs, and ocean heat content (OHC) remains a critical yet less explored
106 aspect, particularly within the Mediterranean context. To improve the prediction of
107 Mediterranean cyclones and mitigate associated risks, a deeper understanding of air-sea
108 interaction processes, specifically surface heat fluxes, momentum fluxes, and upper-ocean
109 thermodynamic responses, and the role of pre-existing oceanic conditions in cyclone genesis
110 and intensification, is essential. Recent studies have increasingly focused on these dynamics,
111 exploring how air-sea exchanges affect not only medicanes intensity but also the ocean's
112 biogeochemical responses (Jangir et al., 2023; Menna et al., 2023; Scardino et al., 2024; Avolio
113 et al., 2024). Notably, Jangir et al. (2023) highlighted the influence of WCEs on the
114 intensification of medicanes, demonstrating that eddy size also plays a critical role; larger
115 eddies tend to promote stronger cyclones and heavier rainfall. In this particular study, we show
116 the influence of eddies and MHW on the intensity of medicane Daniel.

117

118 Most of the studies use the satellite sea level anomaly (SLA) altimetry data from the Copernicus
119 Marine Services (CMEMS) for the detection of eddies. Here, we also use the Surface Water
120 and Ocean Topography (SWOT) satellite data, which are available at high spatial resolution.
121 The SWOT satellite provides the first-ever global observations of ocean dynamics at sub-
122 mesoscale spatial resolutions (1–100 km). While traditional satellite products, such as those
123 from the Copernicus mission, offer spatial resolutions of approximately 25 km globally and
124 12.5 km in the Mediterranean Sea, SWOT's advanced wide-swath altimetry overcomes these
125 limitations by achieving resolutions as fine as 250 m to 2 km. This enhanced capability enables
126 the detection of small-scale ocean features that were previously misrepresented. SWOT
127 observations confirm the widespread presence of sub-mesoscale eddies and internal waves,
128 particularly energetic in regions like western boundary currents and the Antarctic Circumpolar
129 Current (Archer et al., 2025; Tranchant et al., 2025). This high-resolution data is especially
130 valuable for studying ocean-atmosphere interactions, such as the role of eddies in cyclone

131 intensification. In particular, SWOT's ability to capture the structure, intensity, and evolution
132 of eddies provides critical insight into how these features influence heat transport, vertical
133 mixing, and the modulation of cyclone intensity due to eddies. Thus, SWOT marks a
134 transformative step in advancing our understanding of fine-scale ocean processes and their
135 implications for weather, climate, and marine biogeochemistry.

136

137 Atmospheric cyclones are known to trigger substantial phytoplankton blooms (Shang et al.,
138 2015; Chowdhury et al., 2020; Liu et al., 2020). These blooms are primarily attributed to
139 cyclone-induced upwelling and vertical mixing, which transport cold, nutrient-rich, or
140 chlorophyll-loaded water into the euphotic zone, stimulating phytoplankton bloom. Such
141 storm-driven biological responses offer valuable insight into ocean mixing and biogeochemical
142 dynamics (Chen et al., 2022). Additionally, strong cyclonic winds often cause a noticeable
143 decrease in SST, which plays a crucial role in regulating primary productivity (Latha et al.,
144 2015). There are a few studies reported in the other ocean basins that indicate the enhancement
145 of chlorophyll a (Chl-a) concentration following the passage of a cyclone in the presence of
146 eddies (Dutta et al., 2019; Zhang and Qui, 2020; Vidya et al., 2021) and MHW (Oliver et al.,
147 2018; Jangir et al., 2024). Recently, a study by Scardino et al. (2025) reported the response of
148 Mediterranean cyclones on ocean chlorophyll concentration, primarily using Bio-Argo floats.
149 In contrast, our study offers a new perspective by utilizing subsurface profiles of a broader
150 suite of biogeochemical variables, including chlorophyll, phytoplankton, nutrients, and oxygen
151 concentration, complemented by multiple ocean satellite and reanalysis products. To date, such
152 a comprehensive assessment has rarely been reported for the Mediterranean Sea. Here, we
153 investigate the impact of medicane Daniel on ocean biogeochemistry in the context of the SST
154 anomalies along its path.

155

156 In this study, we highlight the co-occurrence of compound extreme events in the region prior
157 to medicane Daniel's landfall. Specifically, we show that the intensification of medicane Daniel
158 may have been driven by the combined influence of a WCE and an MHW. We examine the
159 key atmospheric and oceanic factors that contributed to Daniel's development. The analysis
160 also highlights the unique perspective offered by the SWOT satellite, capturing aspects of air-
161 sea interaction that traditional datasets do not resolve. Additionally, we investigate the
162 medicane's impact on ocean biogeochemistry along its path, and specifically at the WCE
163 location prior to landfall, providing insights into the underlying physical and biological
164 processes that govern such interactions.

165

166 **2. Synoptic evolution and impacts of medicane Daniel:** On September 2-3, a swift cold front
167 traversed Central Europe, generating an upper-level trough that created a cut-off low near
168 Greece by September 4. Named "Daniel" by the Hellenic National Weather Service, this
169 cyclone brought severe thunderstorms to Greece, Turkey, and Bulgaria due to unstable
170 atmospheric conditions and warm waters. Daniel traversed the Mediterranean Sea from 4 to 12
171 September 2023, bringing exceptionally heavy rainfall to Greece and Libya and triggering
172 severe floods and mudslides. While moving south-southwest, Daniel stalled over the central
173 Mediterranean, evolving into a subtropical storm by September 7. By September 9, Daniel
174 transitioned into a tropical-like storm, making landfall in Libya on September 10. Daniel
175 dissipated into a low-pressure trough by September 12 ([Hérincs, 2023](#); [Normand et al., 2024](#)).
176 Medicane Daniel brought intense winds of up to 120 km/h and delivered a total of 240 mm of
177 rainfall over 25 hours ([Normand et al., 2024](#)). It caused catastrophic flash flooding in Derna on
178 September 10, 2023, as torrential rains overwhelmed the river's delta outlet. The flood
179 destroyed large parts of the city's buildings, infrastructure, and bridges, resulting in 8.8 million
180 tons of debris. In Derna alone, 10% of houses were destroyed and 18.5% damaged. In other
181 cities, such as Susah, approximately 28% of homes were destroyed, while Albayda, Al-Marj,
182 and others also suffered heavy losses. Overall, the storm led to 5,898 deaths, 8,000 missing
183 persons, 44,800 displaced individuals, and 18,838 homes damaged across Libya's northeastern
184 coast, making it the deadliest African storm since 1900 ([Hérincs, 2023](#); [Normand et al., 2024](#);
185 [Katsanos et al., 2024](#)).

186

187 **3. Data and Methods:**

188 **3.1 Data sources and products used:**

189 In this study, the best-track data for the medicane Daniel was obtained from the Zivipotty
190 Cyclone Report database (<https://zivipotty.hu/tcr.html>). Eddy identification was based on daily
191 SLA fields sourced from the CMEMS. Specifically, the dataset
192 SEALEVEL_EUR_PHY_L4_NRT_OBSERVATIONS_008_060, with a spatial resolution of
193 0.125°, was utilized. To detect and characterize the MHW, daily SST data from the NOAA
194 Optimum Interpolation SST V2 dataset ([Reynolds et al., 2007](#)) were used. This dataset has a
195 spatial resolution of 0.25° and covers the period from 1981 to the present. The key atmospheric
196 variables, including total column water (which represents the sum of water vapor, liquid water,
197 cloud ice, rain, and snow in a column extending from the surface of the Earth to the top of the
198 atmosphere), total precipitation, vertically integrated moisture divergence, mean sea level

199 pressure (MSLP), 10-meter zonal and meridional wind components, daily radiative fluxes of
200 shortwave and longwave radiations, (denoted as Q_{SW} and Q_{LW} respectively), and turbulent heat
201 fluxes of latent and sensible flux (denoted as Q_{lat} and Q_{sen} respectively) were retrieved from
202 the ERA5 reanalysis (Hersbach et al., 2020). The surface net heat flux (Q_{net}) was derived from
203 a combination of radiative and turbulent fluxes (Menna et al., 2023).

$$204 \quad Q_{net} = Q_{SW} - Q_{LW} - Q_{lat} - Q_{sen} \dots\dots\dots(1)$$

205
206 High-resolution SLA observations were obtained from the SWOT Level 3 satellite product,
207 which offers 2 km spatial resolution, provided by Archiving, Validation and Interpretation of
208 Satellite Oceanographic data (AVISO; [https://www.aviso.altimetry.fr/en/data/products/sea-](https://www.aviso.altimetry.fr/en/data/products/sea-surface-height-products/global/swot-l3-ocean-products.html)
209 [surface-height-products/global/swot-l3-ocean-products.html](https://www.aviso.altimetry.fr/en/data/products/sea-surface-height-products/global/swot-l3-ocean-products.html)).

210 Lastly, biogeochemical variables such as chlorophyll, phytoplankton, nutrients, and dissolved
211 oxygen were accessed via the CMEMS from the product
212 [MEDSEA_MULTIYEAR_BGC_006_008](https://doi.org/10.25423/cmcc/medsea_multiyear_bgc_006_008), available at a 4-5 km spatial resolution, and 1-hr
213 temporal resolution (
214 https://doi.org/10.25423/cmcc/medsea_multiyear_bgc_006_008_medbfm3). Daily satellite-
215 derived chlorophyll products (OCEANCOLOUR_MED_BGC_L4_NRT) with a spatial
216 resolution of 1 km were used in this study (Volpe et al., 2019; Volpe et al., 2018; Berthon and
217 Zibordi, 2004). These datasets are archived by the Copernicus Marine Service
218 (<https://doi.org/10.48670/moi-00298>) and are provided by the Italian National Research
219 Council (CNR, Rome, Italy), with data availability from January 2023 to the present. The
220 multi-sensor product integrates observations from SeaWiFS, MODIS, MERIS, VIIRS, and
221 OLCI, and includes key biogeochemical variables such as chlorophyll-a (Chl-a), diffuse
222 attenuation coefficient at 490 nm, and primary production.

223 Despite their advantages, these datasets are subject to uncertainties arising from atmospheric
224 correction errors, cloud contamination, aerosol effects, and reduced accuracy in optically
225 complex coastal waters. In addition, the gap-filling procedure used to generate continuous
226 fields may introduce smoothing in regions with persistent data gaps. Nevertheless, these
227 products provide robust, high-resolution information on surface biogeochemical variability
228 associated with cyclone-induced ocean processes.

229 **3.2 Methods:** In this study, we investigate the intensification, structure, and impacts of
230 medicane Daniel. This section outlines the methodologies used to analyze the oceanic and

231 atmospheric conditions associated with the event. The analysis focuses on key processes
 232 influencing cyclone formation and intensification, including the role of oceanic features such
 233 as WCEs and MHWs, the contribution of ocean heat content as a source of subsurface thermal
 234 energy, and atmospheric variables such as moisture and wind fields. The methods used for the
 235 identification of the sea eddies and MHWs, as well as the computation of ocean heat content,
 236 are described below.

237

238 **3.2.1 Eddy and marine heatwave identification:**

239 Eddy identification in this study followed the approach of Jangir et al. (2021, 2023) and Sun et
 240 al. (2017), based on geostrophic balance equations relating SLA to geostrophic currents. zonal
 241 (u) and meridional (v) velocity components were derived using equations 2, 3, and 4:

242
$$u = -\frac{g}{f} \left(\frac{dh}{dy}\right) \dots\dots\dots(2)$$

243
$$v = \frac{g}{f} \left(\frac{dh}{dx}\right) \dots\dots\dots(3)$$

244
$$V^2 = u^2 + v^2 \dots\dots\dots(4)$$

245

246 where g is the acceleration caused by gravity, f is the Coriolis parameter, h is the SLA, and V is
 247 the geostrophic current speed.

248

249 Eddies were classified by analysing flow circulation and SLA patterns: anti-cyclonic
 250 circulation with a local SLA maximum indicated a WCE, while cyclonic circulation with a
 251 local SLA minimum indicated a cold-core eddy (CCE). This is consistent with previous
 252 findings, where WCEs in the Northern hemisphere exhibited clockwise (anti-cyclonic)
 253 rotation, while CCEs rotated counterclockwise (cyclonic). The relation between anti-cyclonic
 254 eddies and WCEs along the cyclone’s path was also verified by inspecting SST anomalies with
 255 respect to a boxcar average.

256

257 MHWs were identified using the definition by Hobday et al. (2016) and the software developed
 258 by Zhao et al. (2019) (https://github.com/ZijieZhaoMMHW/m_mhw1.0). An MHW is defined
 259 as a period of at least five consecutive days during which the daily SST exceeds the seasonally
 260 varying 90th percentile, based on a climatological reference period (1983–2021). Events
 261 separated by less than three days are treated as a single MHW. Daily SST anomalies were
 262 computed by subtracting the daily climatology. MHW intensity was classified following

263 Hobday et al. (2018) into four categories based on the metric θ , where θ represents the
 264 normalized SST anomaly relative to the climatological threshold. It is defined as:

265
$$\theta = \frac{SST - SST_{climatology}}{SST_{90th\ percentile} - SST_{climatology}} \dots\dots\dots(5)$$

266 where SST is the daily sea surface temperature, $SST_{climatology}$ is the climatological mean SST,
 267 and $SST_{90th\ percentile}$ is the seasonally varying 90th percentile threshold. Based on this metric,
 268 MHW intensity is categorized as follows: moderate ($1 \leq \theta \leq 2$), strong ($2 \leq \theta \leq 3$), severe ($3 \leq$
 269 $\theta \leq 4$), and extreme ($\theta \geq 4$).

270 **3.2.2 Computation of ocean heat content**

271 We have also calculated the OHC to assess the role of subsurface heat accumulation in driving
 272 compound extreme events, such as the co-occurrence of MHWs and cyclones. Since the ocean
 273 acts as a key energy source for cyclones by supplying heat and moisture, the passage of a
 274 cyclone typically extracts heat from the upper ocean, leading to a decrease in OHC. In this
 275 study, OHC is defined as the vertically integrated thermal energy from the surface down to the
 276 depth of the 20 °C isotherm (a proxy for the thermocline layer). The OHC was computed for
 277 the medicane using the following formulation (Equation 6):

278
$$OHC = \int_{h1}^{h2} \rho C_p T dz \dots\dots\dots(6)$$

279 where ρ is the density of the seawater, C_p is the specific heat capacity of the seawater at
 280 constant pressure, p , $h1$ is the surface, $h2$ is the bottom depth, and T is the temperature in °C.
 281 This approach allows us to quantify how much thermal energy is available in the upper ocean
 282 to potentially intensify cyclones and how this energy is depleted following cyclone passage.

283 **3.2.3 Computation of Ekman pumping**

284 Ekman pumping was computed using the wind stress components $\tau=(\tau_x, \tau_y)$ from ERA5,
 285 namely Eastward Wind Stress (EWSS) and Northward Wind Stress (NSSS), which is available
 286 for $0.25^\circ \times 0.25^\circ$ and hourly temporal resolution. To compute the wind stress curl ($\nabla \times \tau$), the
 287 spatial derivatives of wind stress are used, and it is computed using equation 7:

288
 289
$$curl(\tau) = \frac{\partial \tau_y}{\partial x} - \frac{\partial \tau_x}{\partial y} \dots\dots\dots(7)$$

290
291
292
293
294
295
296
297
298
299
300
301
302
303
304
305
306
307
308
309
310
311
312
313
314
315
316
317
318
319
320
321

The wind stress curl ($\nabla \times \tau$) was calculated using finite-difference estimates of spatial gradients on a latitude-longitude grid, with grid spacing converted to metric units. No additional smoothing was applied to the wind stress fields prior to curl computation. Then, the Ekman pumping velocity (w_e), introduced by Stern (1965) to account for the effect of the ocean currents on upwelling, is calculated using equation 8:

$$w_e = \frac{1}{\rho} \times \text{curl}\left(\frac{\tau}{f+\zeta}\right) \dots \dots \dots (8)$$

This vertical velocity reflects the upwelling (positive w_e) or downwelling (negative w_e) of water, and is a crucial mechanism through which cyclones influence oceanic nutrient transport, mixing, and biological productivity (Li et al., 2021). Here, the relative vorticity (ζ) was computed from the zonal (u) and meridional (v) components of the surface current, as given in Equation (9):

$$\zeta = \frac{\partial v}{\partial x} - \frac{\partial u}{\partial y} \dots \dots \dots (9)$$

The Ekman transport vector components were computed from the wind stress and Coriolis parameter as:

$$M_x = \frac{\tau_y}{\rho(f+\zeta)} \dots \dots \dots (10)$$

$$M_y = \frac{\tau_x}{\rho(f+\zeta)} \dots \dots \dots (11)$$

where ρ is seawater density, and f is the Coriolis parameter (dependent on latitude). The vector field $M=(M_x, M_y)$ was visualized using quiver plots to reveal the spatial structure and directional response of Ekman transport to cyclone wind forcing.

3.2.4 Computation of various properties along the track of medicane Daniel

To estimate the medicane’s characteristic MSLP and wind speed along the cyclone track, we applied Cressman averaging (Cressman, 1959). Once the cyclone center was identified, a spatial average within a 2° radius around the center, weighted by inverse square distance, was computed for MSLP and wind speed. This method captures changes within a 2-degree radius of the cyclone centre, while regions outside this radius are not included. Similarly, daily MHW and high-pass filtered (500 km radius) SST and OHC anomalies, along with their along-track

322 evolution during medicane Daniel, were calculated using a 2-degree search radius and the
323 Cressman interpolation technique. This analysis allows quantification of the relative extremity
324 of the oceanic conditions encountered during intensification. The approach was used to assess
325 variations in cyclone intensity along its path and has been widely employed in previous studies
326 (Jangir et al., 2023).

327

328 **4. Results and discussion**

329 In this section, we present the results of our study on medicane Daniel, focusing on two primary
330 aspects. First, we analyze the influence of pre-existing oceanic conditions, specifically WCEs
331 and MHW conditions, on the cyclone's intensification. Second, we investigate the medicane's
332 impact on ocean biogeochemistry, particularly the observed increase in surface productivity as
333 indicated by enhanced biogeochemical variables. Our findings also explore the physical
334 mechanisms behind these changes, highlighting the interactions between the ocean and
335 atmosphere throughout the lifecycle of medicane Daniel.

336 *4.1 Role of oceanic features in intensification of medicane Daniel*

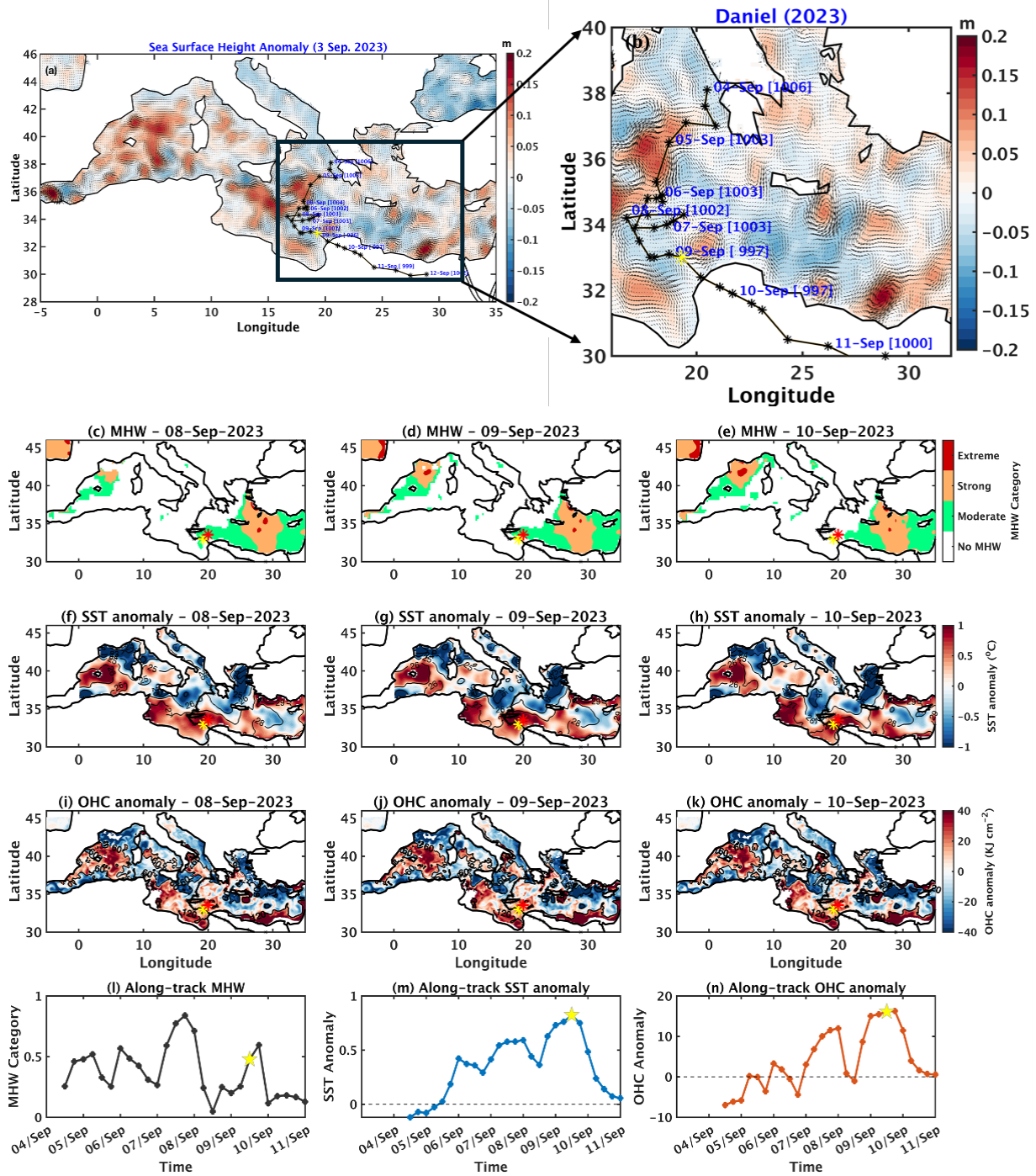
337 Figure 1a-b shows the SLA along the medicane's track. At first, the medicane passed over a
338 cluster of three anticyclonic eddies between September 4 and 6, presumably contributing to its
339 intensification (Jangir et al., 2023). This intensification between 8 and 10 September was also
340 supported by the presence of a moderate MHW, as shown in Figure 1c–e (see also SI Figure
341 1). Furthermore, just before making landfall, the medicane arrived in a region characterized
342 mostly by anticyclonic mesoscale WCE activity (figure 1f–h). OHC anomaly shown in Figure
343 1i–k indicates higher heat content in the southern part of the domain close to landfall location,
344 also supporting the intensification of the medicane. In addition to the maps in panels c–k of
345 Figure 1, the analysis was carried out by computing MHW, SST, and OHC anomalies at each
346 6-hourly track position (Figure 1l–n), with particular emphasis on the maximum cyclone
347 intensity (Max-CI) location. We observed from the analysis that the maximal values of MHW
348 (~ 0.6), SST (~ 0.83 °C), and OHC (~ 16.30 KJ/cm²) anomalies occurred in the last two days
349 before Max-CI, indicating that medicane Daniel intensified over thermodynamically
350 favourable conditions that were among the most anomalous along its track.

351 The combination of two extreme oceanic preconditions, namely the WCE and the MHW,
352 together with high absolute values of OHC at the intensification site near the coastal region,

353 may have contributed to the deadly outcome of this medicane. Rathore et al. (2022) and Jangir
354 et al. (2024) highlighted the critical role of sudden intensification in Cyclone Amphan over the
355 Indian Ocean and medicane Ianos over the Mediterranean Sea, respectively, in the presence of
356 MHWs along their paths. The findings of the current study are consistent with these
357 observations, demonstrating that while cyclone genesis and intensification can occur
358 independently of such features, the presence of WCEs and MHWs may enhance the rate and
359 magnitude of intensification over a shorter time.

360 Figure 1 also highlights the potential importance of ocean characteristics such as WCEs and
361 MHWs in cyclone intensification, indicating that cyclone intensity increased in the presence of
362 WCEs and MHWs. This behavior is similar to how cyclones in other ocean basins react to
363 changes in intensification factors related to underlying eddies (Ali et al., 2007; Lin et al., 2013;
364 Jangir et al., 2020; Jangir et al., 2023). When a cyclone encounters a WCE, the negative
365 feedback loop between cyclone intensity and SST diminishes. Normally, cyclones extract heat
366 from the ocean, resulting in surface cooling due to enhanced mixing and evaporation, which
367 acts to reduce cyclone intensity. However, if a WCE or MHWs are present, the high SST
368 persists longer, intensifying the cyclone and reducing the negative feedback effect (Bender et
369 al., 1993; Jangir et al., 2024).

370 Furthermore, atmospheric cyclones draw a significant portion of their energy from warm, deep
371 ocean waters; therefore, quantifying the amount of this warm, deep water provides a more
372 accurate measure of the energy available to the storm. OHC serves as this metric, indicating
373 how much warm water a cyclone can convert into energy. Studies have shown that OHC is a
374 far superior predictor compared to SST alone (Wada & Usui, 2007; Sharma and Ali, 2014; Lin
375 et al., 2013; Law et al., 2011). Analysis of the OHC revealed a significant amount of OHC at
376 the intensification locations, providing a favorable upper-ocean thermal reservoir for medicane
377 Daniel to intensify. Approximately 120 KJ/cm² of heat was available from September 4th to 9th,
378 even before the cyclone's intensification (Figure 1i-k & SI Figure 2). This accumulated heat at
379 the intensification location is attributed to the presence of the WCE and the MHW, which
380 decreases after the passage of the medicane on the 11th and 12th of September, 2023 (SI Figure
381 2). The presence of heat in the form of SST anomaly (Figure 1f-h) and OHC anomaly (Figure
382 1i-k) along the path of medicane maintains intensity by reducing negative feedback that occurs
383 due to the passage of the cyclone (Jangir et al., 2023; Jangir et al., 2024).



384

385 *Figure 1: (a, b) Sea level anomaly (shading) with geostrophic currents (arrows). The medicane*
 386 *track is overlaid on (c-e) marine heatwave (MHW), (f-h) sea surface temperature (SST)*
 387 *anomalies (500 km radius high pass filter), and (i-k) ocean heat content (OHC) anomalies (500*
 388 *km radius high pass filter). In panels f-k, absolute values are indicated by contours. Panels (l-*
 389 *n) show along-track values of MHW, SST, and OHC anomalies. The yellow stars (pentagon)*
 390 *in panels a-k (l-n) mark the location of maximum cyclone intensity (Max-CI), while the red*
 391 *pentagons mark the Max-CI location defined by the minimum mean sea level pressure. The red*

392 *star marker in panels c-k indicates the position of the WCE. Dates for each panel are shown*
393 *along the track.*

394

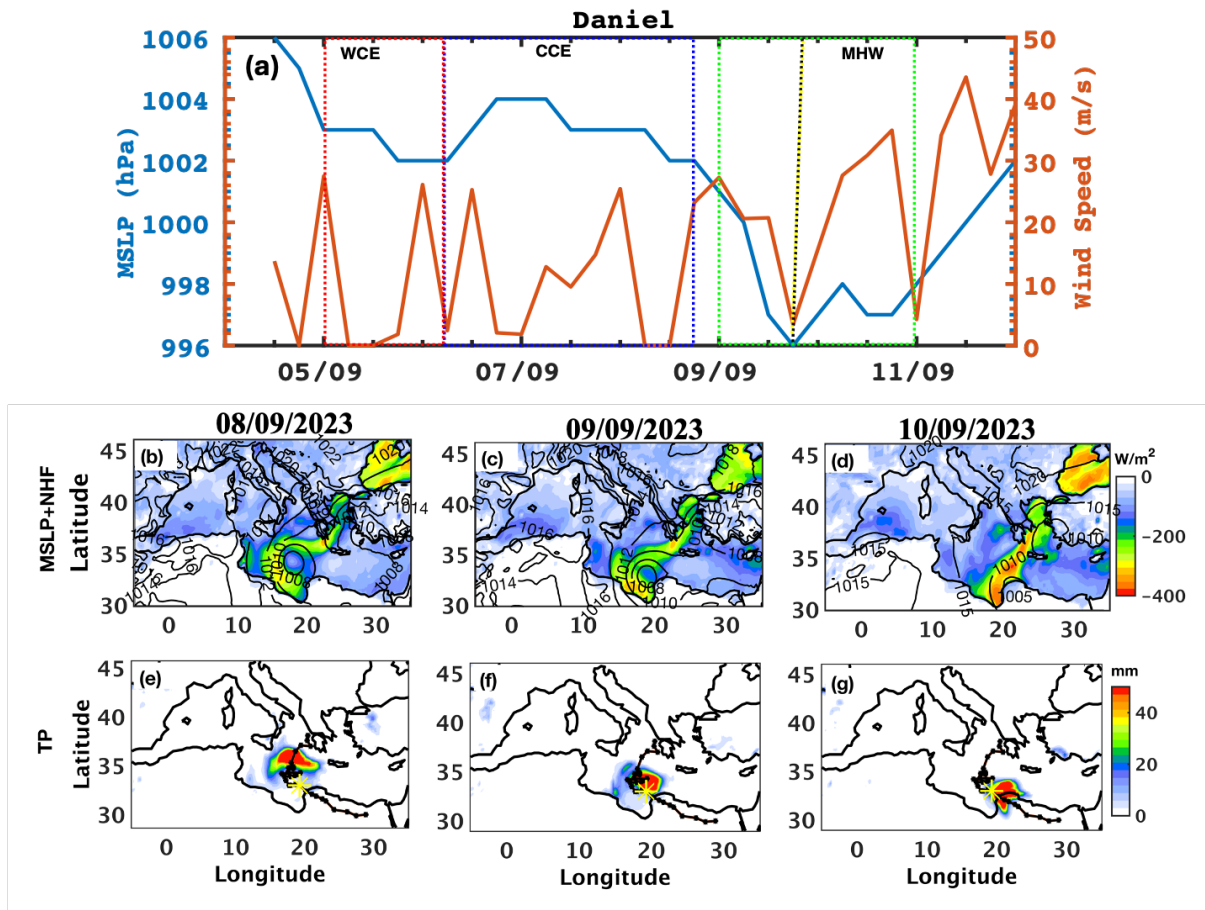
395 ***4.2 The role of atmospheric precursors in the intensification of medicane Daniel***

396 The MSLP and wind speed, computed using the Cressman averaging method (Cressman, 1959)
397 along the cyclone's track, are shown in Figure 2a. The MSLP indicates moderate intensification
398 from 1006 hPa to 1002 hPa when the storm passes over the WCE on 5 September 2023 (Figure
399 2a). Subsequently, from the 6th to the 7th September 2023, the medicane passes over a CCE
400 region, and its intensity is reduced to 1004 hPa. Upon reaching the vicinity of Libya's coast on
401 8 September 2023, it quickly intensified. An additional WCE was present in the vicinity of the
402 cyclone's path at that time, potentially further contributing to its fast intensification. This fast
403 intensification is indicated by a drop in the MSLP and a sudden increase in wind speed near
404 the eddy and MHW location (Figure 2a). The cutoff low, which was supported by high net heat
405 flux, persisted for two days (Figures 2b-d, SI Figure 3), even after the cyclone made landfall in
406 Libya.

407 Moisture processes play an equally important role in cyclone intensification. Their importances
408 been demonstrated in previous studies by Jangir et al. (2023) and Pytharoulis et al. (2018),
409 emphasizing that elevated SST in the form of WCE or MHW is essential for providing moisture
410 to a medicane via surface fluxes, enhancing convection. Additionally, Jangir et al. (2024)
411 highlighted the importance of moisture convergence in the intensification of cyclones and
412 increasing total associated precipitation. Thus, motivated by these findings, we focus in this
413 study on the causes of the intensification of the medicane Daniel and the extreme flood that
414 occurred during the event.

415 The analysis of moisture convergence (i.e., mean vertically integrated moisture divergence)
416 showed a pattern of moisture convergence along the cyclone's path. Notably, this convergence
417 coincides with the eddy location at the intensification location on September 9th, 2023 (SI
418 Figure 4). This alignment suggests that the eddy supplied the moisture needed for the cyclone's
419 intensification. The interaction between the eddy and the medicane likely enhanced moisture
420 availability, contributing to the storm's strengthening at that specific point in its path.
421 Additionally, the total column water was notably high at the WCE and MHW locations. While
422 this total water was present before the intensification location as well, it converged around the
423 eddy at the intensification location (SI Figure 5), leading to substantial precipitation in that area

424 (Figure 2e-g and SI Figure 6). The severe precipitation near the coastal region highly coincides
 425 with the WCE and MHW. The WCE's influence intensified the cyclone by providing additional
 426 moisture and heat, leading to heavy rainfall. This heavy precipitation, concentrated near the
 427 coast, exacerbated the storm's impact, severely damaging the affected areas.



428
 429 *Figure 2: (a) Mean sea level pressure (MSLP), and wind speed computed using the Cressman*
 430 *average along the track of the medicane Daniel. The red, blue, and green boxes indicate the*
 431 *locations of the warm-core eddy (WCE), cold-core eddy (CCE) and marine heatwave (MHW),*
 432 *respectively. The medicane track is overlaid on (b-d) the daily mean of MSLP (contours) net*
 433 *heat fluxes (shading; positive downward), and on (e-g) total precipitation for 8-10 September*
 434 *2023. The yellow star indicates the location of maximum intensification (Max-CI).*

435

436 **4.3 SWOT satellite data**

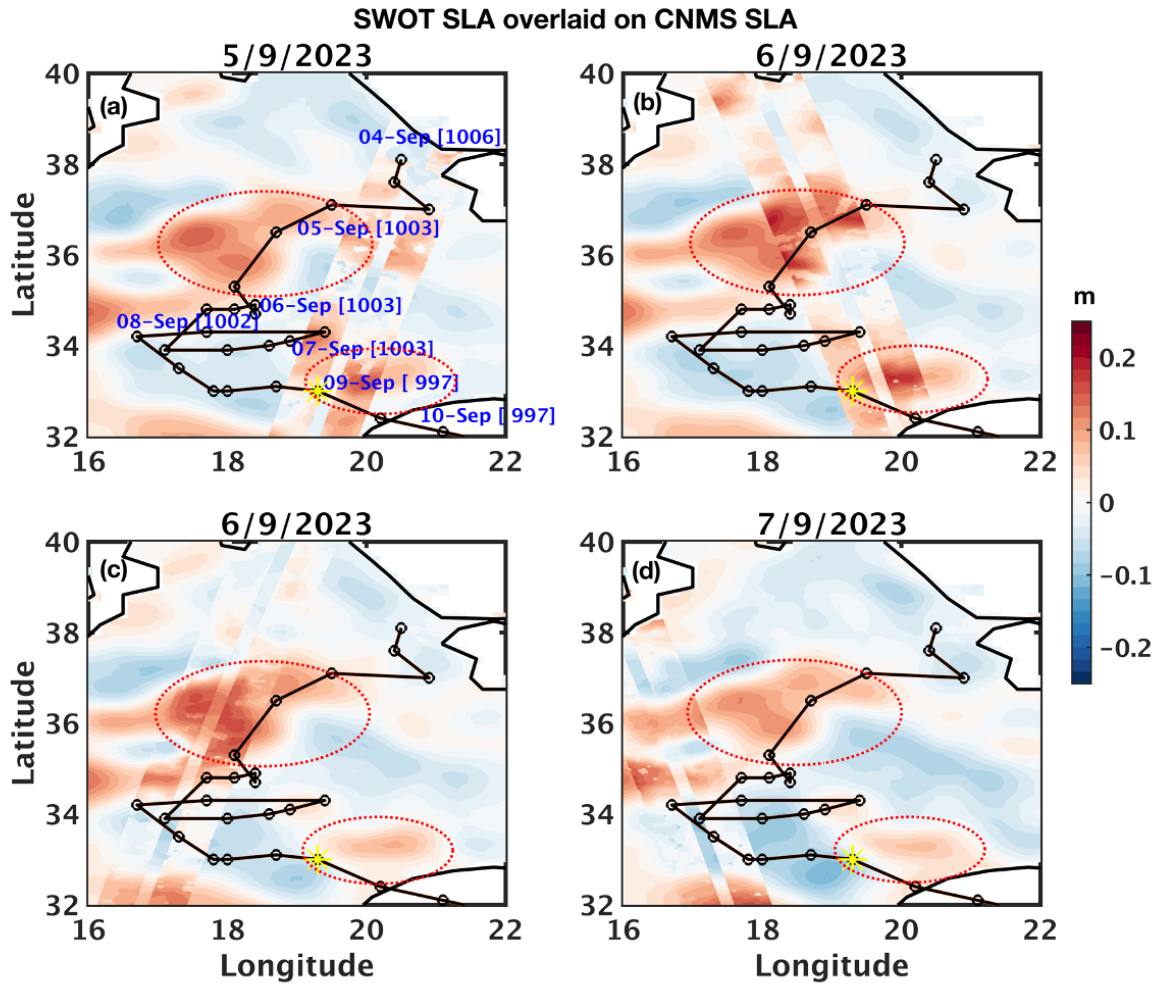
437 The SWOT mission offers high-resolution sea surface height anomaly or SLA data with
 438 unprecedented spatial detail, enabling precise detection of mesoscale and sub-mesoscale ocean
 439 features, such as eddies and fronts (Morrow et al., 2019). This can be valuable for studying
 440 cyclones, which interact strongly with oceanic eddies that influence storm intensity. Unlike
 441 traditional altimeters, SWOT's wide-swath coverage enables improved detection of mesoscale

442 and sub-mesoscale eddies, frontal gradients, and filaments that regulate ocean heat distribution
443 and air-sea exchanges. These features are often underrepresented in low-resolution datasets,
444 limiting their ability to capture localized processes such as eddy-cyclone interactions and
445 cyclone-induced mixing. By improving the detection of these fine-scale physical structures,
446 SWOT also provides a framework for interpreting biogeochemical responses. While coarse
447 datasets show bulk chlorophyll changes, SWOT helps identify localized regions of enhanced
448 mixing and upwelling that drive nutrient supply and biological variability. This allows for a
449 clearer linkage between physical forcing and biogeochemical response. Overall, SWOT
450 overcomes key limitations of conventional altimetry by preserving high-frequency spatial
451 gradients, enabling a more accurate representation of the ocean state during extreme events
452 such as medicane Daniel.

453

454 Here we show the SWOT swath passing over the location of the eddies along the track of
455 medicane Daniel (Figure 3). In Figures 3a-b, the eddy initially appears small and low intensity
456 in the CMEMS, and the cyclone is observed nearby. However, SWOT data reveal a more
457 intense and extensive eddy structure than CMEMS, with the cyclone positioned directly above
458 it. These findings report the value of SWOT observations in capturing fine-scale oceanic
459 features and dynamics, offering critical insights into cyclone-eddy interactions.

460



461

462 *Figure 3: (a-d) The SWOT sea level anomaly (SLA) swath (2 km resolution) overlaid on SLA*
 463 *from CMEMS (12.5 km spatial resolution). The dates shown above each panel correspond to*
 464 *the periods of SWOT swath data availability.*

465

466 **4.4 Impact of medicane Daniel on ocean biogeochemistry**

467 To investigate the impact of the medicane on oceanic physical (temperature and salinity) and
 468 biogeochemical properties (i.e., chlorophyll-a, phytoplankton, nitrate and phosphate, and
 469 oxygen concentration), we analyzed vertical profiles of key variables along the cyclone's track.

470 The analysis focused on differences between two days after the cyclone's passage, minus two
 471 days before (Figure 4a-g). The results reveal a notable decrease in temperature along the

472 cyclone path, with a general strong cooling along its path except for a short pause in the cold
 473 SST anomaly region in the morning of the 8th (Figure 1n). This region was also relatively

474 outside the MHW domain (Figure 1l). The salinity also decreases on the surface presumably
 475 due to a massive influx of freshwater from heavy rainfall, again, except for the morning of the

476 8th, in which the cyclone was outside the influence of WCEs and MHW (Figure 4b). In
 477 contrast, at the subsurface, Chl-a and phytoplankton concentrations exhibit a marked dipole

478 (Figure 4c-d), while nutrients increase (Figure 4e-f) and oxygen decreases (Figure 4g). This
479 biological response can be attributed to cyclone-induced Ekman pumping upwelling and high
480 subsurface vertical mixing. Enhanced nutrient availability at the subsurface layer can persist
481 into the mixed layer, allowing for sufficient sunlight, and together with elevated oxygen
482 concentrations (associated with surface cooling), may foster increased surface Chl-a and
483 phytoplankton biomass. Signs of this can be seen in the MHW region, where higher Chl-a
484 concentrations reach the surface. But, unlike previous results (Jangir et al., 2026), medicane
485 Daniel only shows an increase in Chl-a at the surface in the MHW region.

486

487 Profiles of temperature and Chl-a at the maximum cyclone intensity (Max-CI) location and
488 time (Figure 4h-i) reveal general cooling after the passage of the cyclone. The deep chlorophyll
489 maximum (DCM) was located far below the mixed layer depth, at around 140m depth. The
490 subsurface crossings between the profiles and the relatively stationary location of the DCM in
491 Figure 4i indicate that out of the two processes mentioned above, namely cyclone-induced
492 upwelling and high subsurface vertical mixing, only cyclone-induced subsurface mixing can
493 explain the change. Subsurface mixing mechanism is typically much slower than turbulence in
494 the mixed layer, but under storm conditions may become comparable. The gradual subsurface
495 increase in Chl-a, as opposed to the vertical line observed in the mixed layer, indicates weaker
496 but comparable turbulence below the mixed layer.

497

498 Figure 4i shows the change in subsurface profiles at the time and location of Max-CI, situated
499 on the periphery of a WCE. To further investigate the underlying mechanisms and compare the
500 medicane's impact on both WCEs and CCEs, vertical cross-sections across the main center of
501 the WCE and adjacent CCE region were analyzed during the pre-storm, during storm, and post-
502 storm phases (Figure 5). These cross-sections reveal notable eddy-dependent subsurface
503 changes associated with the passage of the medicane. As expected, during and after the passage
504 of the storm, significant surface cooling is observed in Figure 5 (panels b-d and h-i). In addition
505 to the cooling observed within the mixed layer, three distinct circular-like cooling patterns are
506 evident immediately beneath it. These may indicate a secondary circulation starting at the deep
507 subsurface (below 200m), which transfers deep cold water to the layers below the mixed layer.
508 In this case, the two patterns on the right indicate an upwelling cell at the WCE boundaries
509 (green arrows in Figure 5i) and another at the CCE center (purple arrow in Figure 5i). These
510 circulation cells also create the dipole pattern in the Chl-a inside the WCE and the CCE (Figure
511 5, panels e-g and j-k).

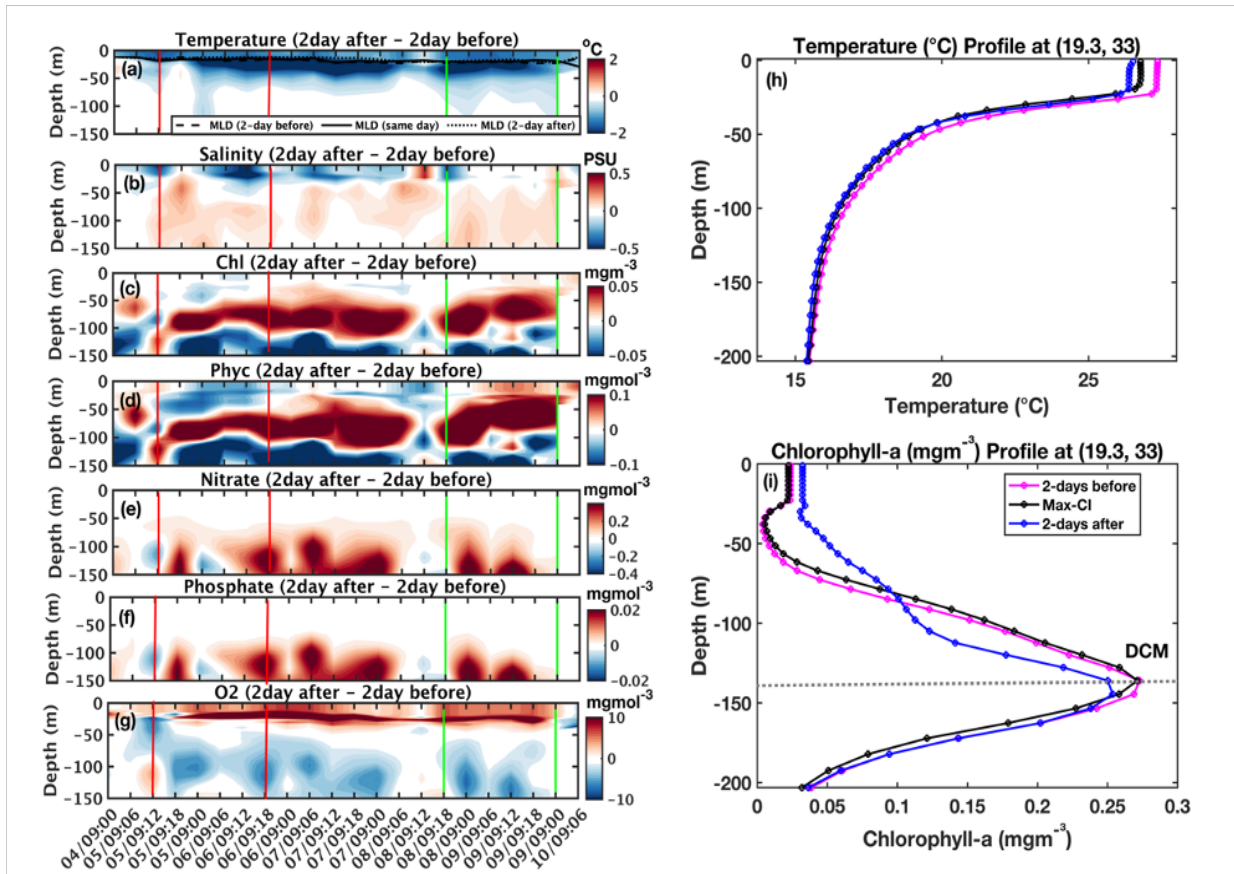
512

513 To explore the dynamical mechanisms, Figure 6 shows vertical profiles from 1 to 15 September
514 2023 of Chl-a at two locations along the same line as in Figure 5a, one inside the CCE (panel
515 a) and the other inside the WCE (panel b). Before the arrival of the medicane (1-5 September),
516 the DCM within the CCE was shallower than in the WCE, consistent with the typical vertical
517 structure of these eddies. The DCM in both eddies remains relatively stable until the cyclone
518 approaches the region. As the medicane approaches the eddies, it intensifies the CCE while
519 diminishing the WCE, which, as expected from theory (e.g., [Klein & Lapeyre, 2009](#)), supports
520 eddy-induced upwelling. Indeed, during the storm, the DCM is lifted upward in both cases
521 from 5 to 9 September. Yet, the DCM inside the WCE is exhibited significantly greater
522 shoaling than inside the CCE ($\sim 40\text{m}$ in the WCE relative to $\sim 15\text{m}$ in the CCE). The more
523 pronounced response in the WCE likely stems from lower thermal stratification and higher
524 surface wind stress curl that contribute to cyclone-induced Ekman pumping upwelling. Only a
525 few days later, the DCM inside the WCE partially starts to restore its pre-storm condition. The
526 DCM inside the CCE quickly drops back down and even overshoots its depth relative to pre-
527 storm conditions, which can be explained by its stronger stratification and resulting buoyancy
528 restoring force. In addition, we found that cyclone-induced upwelling alone cannot explain the
529 DCM increase in both the WCE and CCE (Figure 6c), which indicates an increase of about 10-
530 15 meters during the medicane influence (5-9 September). Therefore, we conclude that the
531 upwelling may have also been influenced by isopycnal adjustment triggered by the medicane.

532

533 Subsurface mixing similar to what was shown under the medicane at Max-CI (Figure 4i), seems
534 to play a role also here. This role can be indicated by the crossing of the Chl-a profiles during
535 the storm (5-9 September) with the profiles after the storm (10-15 September) between MLD
536 ($\sim -20\text{m}$) and the DCM ($\sim -130\text{m}$). However, here, it seems to complement upwelling and to
537 play a more important role at the WCE (as expected, since in general wind stress is higher
538 above WCEs). Also, satellite-based surface observations (Figure 6d) indicate higher Chl-a
539 above the WCE region, which may be explained by the closer-to-the-surface DCM and stronger
540 cyclone-induced upwelling and vertical mixing.

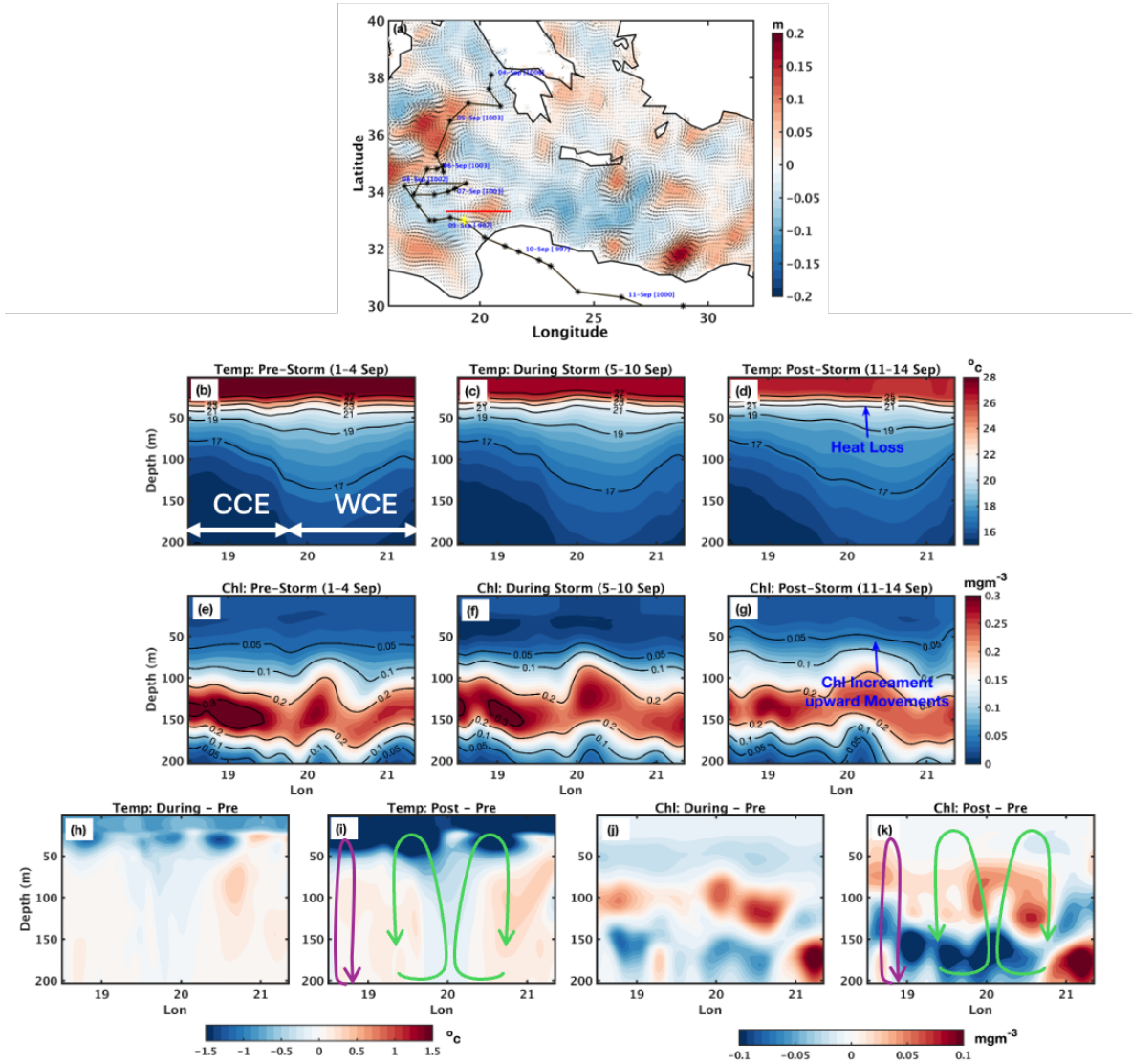
541



542

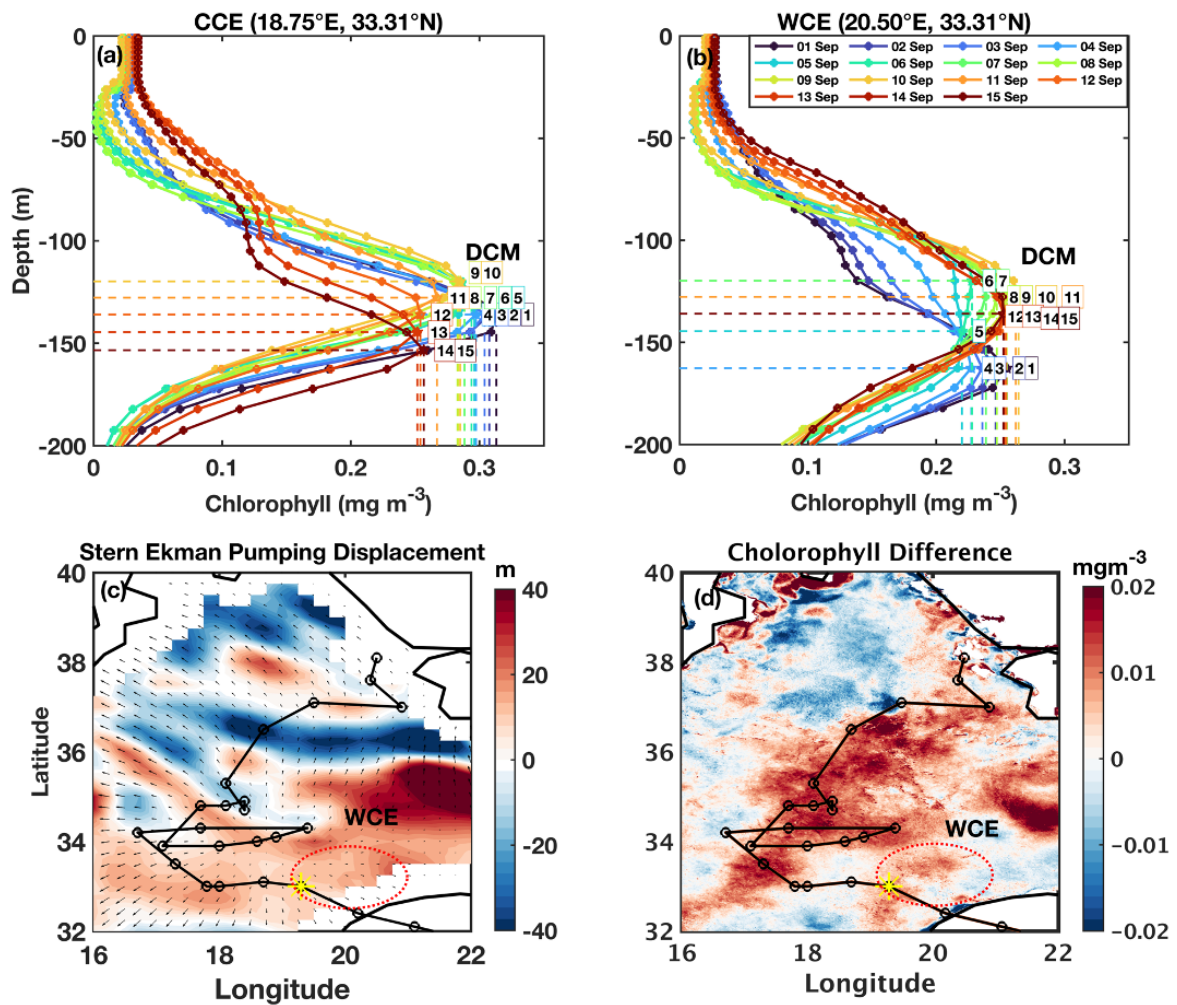
543 *Figure 4: Profiles of physical (a-d) and biogeochemical (e-g) variables along the track of*
 544 *medicane Daniel. The left panels show the difference between two days after and two days*
 545 *before the event. Red and green vertical lines in panels (a-g) delineate the location of the warm-*
 546 *core eddy (WCE) and marine heatwave (MHW) along the track, respectively. The black line in*
 547 *the temperature profile indicates the mixed layer depth.*

548



549
 550
 551
 552
 553
 554
 555
 556
 557
 558
 559
 560
 561
 562
 563
 564

Figure 5: (a) Sea level anomaly with a red line indicating the section across the second warm-core eddy (WCE) used in subsequent panels. (b-d) Temperature profiles and isotherms before, during, and after the medicane along this section. (e-g) Chlorophyll-a profiles before, during, and after the medicane along the same section. (h-i) Temperature differences (during-storm minus pre-storm, and post-storm minus pre-storm). (j-k) Same as (h-i), but for Chlorophyll-a. Green arrows denote the location of a secondary circulation cell, and the purple arrow indicates subsurface mixing.



565
566

567 *Figure 6: Chlorophyll-a profiles from 1 to 15 September 2023 at the cold-core eddy (CCE; a)*
 568 *and warm-core eddy (WCE; b) locations. (c) Cumulative Ekman pumping displacement for 5–*
 569 *9 September 2023, with arrows indicating the transport vector during the cyclone. (d) Satellite*
 570 *chlorophyll-a (2 km spatial resolution) before and after medicane Daniel. The red dotted*
 571 *ellipse indicates the location of the WCE, and the yellow star denotes the location of maximum*
 572 *cyclone intensity (Max-CI).*

573

574 5. Conclusions

575 This case study provides comprehensive insights into the intensification and impacts of
 576 medicane Daniel, which developed over the Mediterranean Sea in September 2023. The
 577 findings show the significant role of oceanic and atmospheric variables in cyclone
 578 intensification, particularly the presence of WCE and MHW (Figure 7). These oceanic features
 579 reduced the negative feedback loop between cyclone intensity and SST, allowing the cyclone
 580 to maintain and even increase its intensity. This study also highlighted the importance of OHC

581 in providing the energy necessary for cyclone intensification, with approximately 120 KJ/cm²
582 of heat available at the intensification location over the WCE and MHW. Additionally, the
583 convergence of moisture at the locations of the WCE and MHW, combined with the elevated
584 total water column, contributed to the heavy precipitation observed in the coastal areas in
585 Libya.

586

587 This study highlights the critical role of high-resolution SWOT data in advancing our
588 understanding of air-sea interaction processes. While CMEMS data, with its coarser spatial
589 resolution, suggests the presence of a weak eddy near the cyclone intensification region,
590 SWOT's finer 2 km resolution reveals a high-intensity WCE precisely aligned with the
591 cyclone's path. This enhanced detection capability provides a more accurate illustration of eddy
592 characteristics and their influence on cyclone dynamics. Furthermore, satellite-derived Chl-a
593 data indicate an enhanced bloom over the WCE location, supported by positive Ekman
594 pumping values. These high values indicate cyclone-induced upward movement of water from
595 deeper layers to the surface, bringing cold, nutrient-rich water to the surface, and boosting
596 ocean productivity.

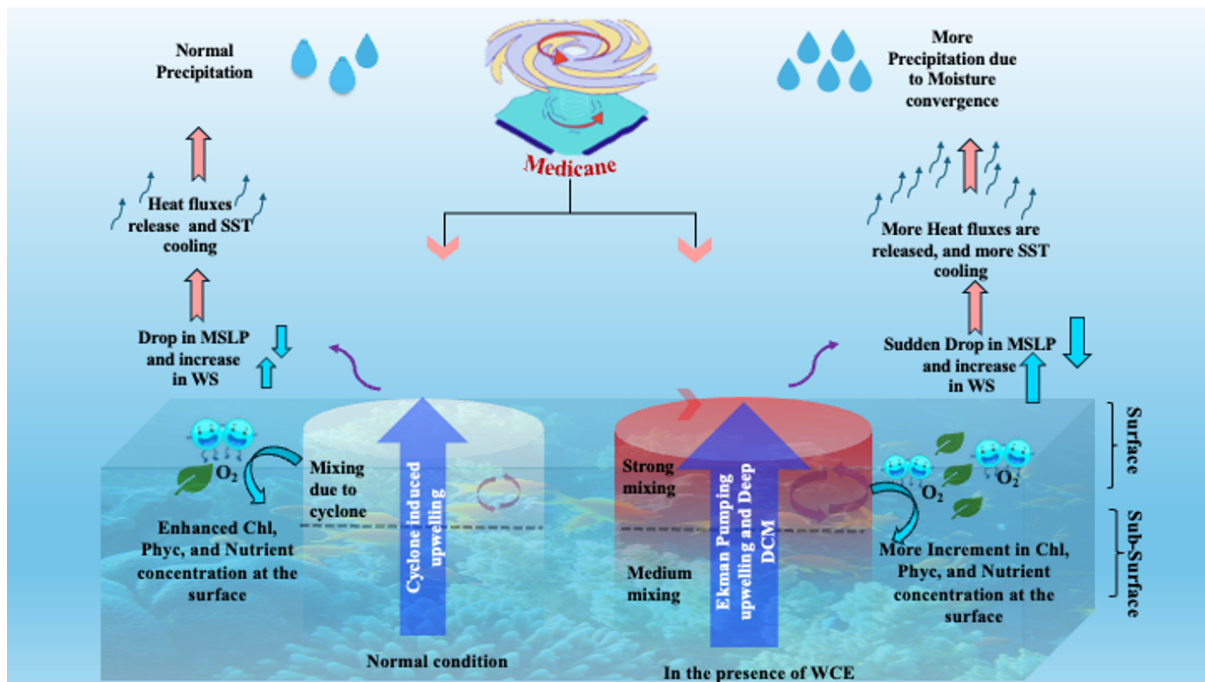
597

598 Subsurface profiles of physical and biogeochemical properties show a notable temperature
599 decrease above the mixed layer depth, particularly over the WCE and MHW regions. The
600 passage of the cyclone triggers vertical mixing, leading to an increase in surface nutrient
601 concentrations. Combined with sufficient sunlight in the euphotic zone, this promotes a surge
602 in surface Chl-a and phytoplankton productivity. Cross-sectional analysis further reinforces
603 these findings: a clear upward shift in isotherms following the cyclone indicates heat loss and
604 active upwelling over the WCE. Concurrently, the Chl-a sections display an upward
605 displacement and intensification of Chl-a concentrations, confirming the strong
606 biogeochemical response induced by the cyclone's passage over the WCE region.

607

608 In conclusion, the study of medicane Daniel emphasizes the need for a deeper understanding
609 of both oceanic and atmospheric factors in predicting and mitigating the impacts of such
610 cyclones in the Mediterranean region. The findings suggest that, similar to tropical cyclones in
611 other ocean basins, medicanes are significantly influenced by the interplay of oceanic heat
612 content, eddies, and atmospheric dynamics. These factors are responsible for the intensification
613 of the cyclone and the destruction caused by the medicane.

614



615
 616 *Figure 7: Schematic illustrating the process associated with cyclone intensification over warm-*
 617 *core eddy and marine heatwave, and their impact on ocean biogeochemistry.*
 618
 619

620 **Data Availability:**

621
 622 Data can be Archived from the links below-

623 https://doi.org/10.25423/cmcc/medsea_multiyear_bgc_006_008_medbfm3

624 <https://doi.org/10.48670/moi-00298>

625 <https://zivipotty.hu/tcr.html>

626 [https://www.aviso.altimetry.fr/en/data/products/sea-surface-height-products/global/swot-13-](https://www.aviso.altimetry.fr/en/data/products/sea-surface-height-products/global/swot-13-ocean-products.html)
 627 [ocean-products.html](https://www.aviso.altimetry.fr/en/data/products/sea-surface-height-products/global/swot-13-ocean-products.html)

628
 629 **Author Contributions:**

630 B.J. contributed to the conceptualization of the study, data curation, formal analysis, and
 631 writing of the original draft.

632
 633 E.S. served as the project investigator, contributed to conceptualization, provided resources
 634 and software support, supervised the research, and contributed to review, and editing, as well
 635 as funding acquisition.

636
 637 **Competing Interests:** The authors declare no conflict of interest.

638 **Acknowledgments:** The authors acknowledge the data-providing agencies (i.e., CMEMS,

639 AVISO) for providing data free of cost.

640 **Funding:** This research was supported by the Israel Science Foundation (Grant 2228/21).

641

642 **References**

643 Ali, M. M., Jagadeesh, P. S. V. and Jain, S., 2007. Effects of eddies on Bay of Bengal cyclone intensity,
644 *Eos Trans. AGU*, 88(8), 93–95, doi:[10.1029/2007EO080001](https://doi.org/10.1029/2007EO080001).

645

646 Archer, M., Wang, J., Klein, P. *et al.*, 2025. Wide-swath satellite altimetry unveils global submesoscale
647 ocean dynamics. *Nature* 640, 691–696. <https://doi.org/10.1038/s41586-025-08722-8>

648

649 Avolio, E., Fanelli, C., Pisano, A., & Miglietta, M. M. 2024. Unveiling the relationship between
650 Mediterranean tropical-like cyclones and rising Sea Surface Temperature. *Geophysical Research*
651 *Letters*, 51, e2024GL109921. <https://doi.org/10.1029/2024GL109921>

652

653 Bender, M. A., Ginis, I., and Kurihara, Y., 1993. Numerical simulations of tropical cyclone-ocean
654 interaction with a high-resolution coupled model, *J. Geophys. Res.*, 98(D12), 23245–23263,
655 doi:[10.1029/93JD02370](https://doi.org/10.1029/93JD02370).

656

657 Berthon, J.-F., Zibordi, G., 2004. Bio-optical relationships for the northern Adriatic Sea. *Int. J. Remote*
658 *Sens.*, 25, 1527-1532.

659

660 Chen, Y., Pan, G., Mortimer, R., Zhao, H., 2022. Possible Mechanism of Phytoplankton Blooms at the
661 Sea Surface after Tropical Cyclones. *Remote Sensing*. 14, 6207. doi: 10.3390/rs14246207

662

663 Cherif, S., Doblás-Miranda, E., Lionello, P., Borrego, C., Giorgi, F., Iglesias, A., et al., 2020. Drivers of
664 change. In *Climate and environmental change in the Mediterranean Basin—current situation and risks*
665 *for the future* (pp. 59–128). First Mediterranean Assessment Report. Union for the Mediterranean, Plan
666 Bleu, UNEP/MAP.

667

668 Chowdhury, R. R., Prasanna Kumar, S., Narvekar, J., & Chakraborty, A., 2020. Back-to-back
669 occurrence of tropical cyclones in the Arabian Sea during October–November 2015: Causes and
670 responses. *Journal of Geophysical Research: Oceans*, 125, e2019JC015836. doi:
671 [10.1029/e2019JC015836](https://doi.org/10.1029/e2019JC015836)

672

673 Claud, C., Alhammoud, B., Funatsu, B. M., and Chaboureaud, J.-P., 2010. Mediterranean hurricanes:
674 large-scale environment and convective and precipitating areas from satellite microwave observations,
675 *Nat. Hazards Earth Syst. Sci.*, 10, 2199–2213, <https://doi.org/10.5194/nhess-10-2199-2010>.

676

677 Cressman, G. P., 1959. An operational objective analysis scheme. *Monthly Weather*
678 *Review*, 87, 367–374. doi: [10.1175/1520-0493\(1959\)087<0367:aoas>2.0.co;2](https://doi.org/10.1175/1520-0493(1959)087<0367:aoas>2.0.co;2)

679

680 Dutta, D., Mani, B. & Dash, M.K., 2019. Dynamic and thermodynamic upper-ocean response to the
681 passage of Bay of Bengal cyclones ‘Phailin’ and ‘Hudhud’: a study using a coupled modelling system.
682 *Environ Monit Assess* 191 (Suppl 3), 808.. <https://doi.org/10.1007/s10661-019-7704-9>.

683

684 Emanuel, K., 2005. Genesis and maintenance of “Mediterranean hurricanes.” *Advances in Geosciences*,
685 2, 217–220. <https://doi.org/10.5194/adgeo-2-217-2005>

686 Fita, L., Romero, R., Luque, A., Emanuel, K., and Ramis, C., (2007) Analysis of the environments of
687 seven Mediterranean tropical-like storms using an axisymmetric, nonhydrostatic, cloud resolving
688 model, *Nat. Hazards Earth Syst. Sci.*, 7, 41–56, <https://doi.org/10.5194/nhess-7-41-2007>.

689
690 Flaounas, E., Raveh-Rubin, S., Wernli, H., Drobinski, P., and Bastin, S., (2015). The dynamical
691 structure of intense Mediterranean cyclones, *Clim. Dynam.*, 44, 2411–2427,
692 <https://doi.org/10.1007/s00382-014-2330-2>
693
694 Flaounas, E.; Davolio, S.; Raveh-Rubin, S.; Pantillon, F.; Miglietta, M.M.; Gaertner, M.A.; Hatzaki,
695 M.; Homar, V.; Khodayar, S.; Korres, G.; et al., 2022. Mediterranean Cyclones: Current Knowledge
696 and Open Questions on Dynamics, Prediction, Climatology and Impacts. *Weather Clim. Dyn.* 3, 173–
697 208
698
699 Flaounas, E., Dafis, S., Davolio, S., Faranda, D., Ferrarin, C., Hartmuth, K., Hochman, A.,
700 Koutroulis, A., Khodayar, S., Miglietta, M. M., Pantillon, F., Patlakas, P., Sprenger, M., and
701 Thurnherr, I.: Dynamics, predictability, impacts and climate change considerations of the
702 catastrophic Mediterranean Storm Daniel (2023), *Weather Clim. Dynam.*, 6, 1515–1538,
703 <https://doi.org/10.5194/wcd-6-1515-2025>, 2025.
704
705 Flocas, H. A., 2000. Diagnostics of cyclogenesis over the Aegean sea using potential vorticity inversion,
706 *Meteorol. Atmos. Phys.*, 73, 25–33, <https://doi.org/10.1007/s007030050061>
707
708 González-Alemán, J. J., Pascale, S., Gutierrez-Fernandez, J., Murakami, H., Gaertner, M. A., & Vecchi,
709 G. A. (2019). Potential increase in hazard from Mediterranean hurricane activity with global warming.
710 *Geophysical Research Letters*, 46, 1754–1764. <https://doi.org/10.1029/2018GL081253>
711
712 Hersbach, H., Bell, B., Berrisford, P., Hirahara, S., Horanyi, A., Muñoz-Sabater, J., et al., 2020. The
713 Era5 global reanalysis. *Quarterly Journal of the Royal Meteorological Society*, 146, 1999–2049, doi:
714 [10.1002/qj.3803](https://doi.org/10.1002/qj.3803).
715
716 Hérincs, D., 2023. *Tropical Storm Daniel: Mediterranean tropical cyclone report (7–10 September*
717 *2023)*. Zivipotty.hu. https://zivipotty.hu/2023_daniel.pdf
718
719 Hobday, A. et al., 2016. A hierarchical approach to defining marine heatwaves. *Prog. Oceanogr.* 141,
720 227–238.
721
722 Hobday, A.J., Oliver, E.C.J., Sen Gupta, A., Benthuisen, J.A., Burrows, M.T., Donat, M.G., Holbrook,
723 N.J., Moore, P.J., Thomsen, M.S., Wernberg, T., and Smale, D.A., 2018. Categorizing and naming
724 marine heatwaves. *Oceanography* 31(2):162–173, <https://doi.org/10.5670/oceanog.2018.205>.
725
726 Hochman, A., Scher, S., Quinting, J., Pinto, J. G., & Messori, G., 2021. A new view of heat wave
727 dynamics and predictability over the eastern Mediterranean. *Earth System Dynamics*, 12(1), 133–149.
728 <https://doi.org/10.5194/esd-12-133-2021>
729
730 IPCC., 2021. In V. Masson-Delmotte, P. Zhai, A. Pirani, S. L. Connors, C. Péan, et al. (Eds.), *Climate*
731 *Change 2021: The Physical Science Basis. Contribution of Working Group I to the Sixth Assessment*

732 *Report of the Intergovernmental Panel on Climate Change*. Cambridge University Press.
733 <https://doi.org/10.1017/9781009157896>
734

735 Jangir B., Mishra A. K., Strobach, E., 2024. The interplay between medicanes and the Mediterranean
736 Sea in the presence of sea surface temperature anomalies, *Atmospheric Research*, Volume 310, 107625,
737 ISSN 0169-8095, <https://doi.org/10.1016/j.atmosres.2024.107625>.
738

739 Jangir, B., Mishra, A. K., & Strobach, E., 2023. Effects of mesoscale eddies on the intensity of cyclones
740 in the Mediterranean Sea. *Journal of Geophysical Research: Atmospheres*, 128, e2023JD038607, doi:
741 [10.1029/2023JD038607](https://doi.org/10.1029/2023JD038607)
742

743 Jangir, B., Swain, D., & Ghose, S., 2021. Influence of eddies and tropical cyclone heat potential on
744 intensity changes of tropical cyclones in the North Indian Ocean. *Advances in Space Research*, 68(2),
745 773–786, doi: [10.1016/j.asr.2020.01.011](https://doi.org/10.1016/j.asr.2020.01.011)
746

747 Jangir, B., Reale, M., Menna, M., Mishra, A. K., Marellucci, R., Cossarini, G., et al. (2026). The
748 response of the physical and biogeochemical marine environment to the passage of Mediterranean
749 cyclones in the presence of eddies, gyres, and marine heat wave. *Journal of Geophysical Research:*
750 *Oceans*, 131, e2025JC023151. <https://doi.org/10.1029/2025JC023151>
751

752 Katsanos, D., Retalis, A., Kalogiros, J., Psiloglou, B. E., Roukounakis, N., & Anagnostou, M., 2024.
753 Performance Evaluation of Satellite Precipitation Products During Extreme Events—The Case of the
754 Medcane Daniel in Thessaly, Greece. *Remote Sensing*, 16(22), 4216.
755 <https://doi.org/10.3390/rs16224216>
756

757 Khodayar, S., Kushta, J., Catto, J. L., Dafis, S., Davolio, S., Ferrarin, C., et al., 2025. Mediterranean
758 cyclones in a changing climate: A review on their socio-economic impacts. *Reviews of Geophysics*, 63,
759 e2024RG000853. <https://doi.org/10.1029/2024RG000853>.
760

761 Klein, P., and Lapeyre, G., 2009. The Oceanic Vertical Pump Induced by Mesoscale and Submesoscale
762 Turbulence. *Annual Review of Marine Science*, 1(Volume 1, 2009):351–375, 2009. ISSN 1941-0611.
763 doi:<https://doi.org/10.1146/annurev.marine.010908.163704>.
764

765

766 Kouroutzoglou, J., Flocas, H. A., Keay, K., Simmonds, I., and Hatzaki, M., 2011. Climatological
767 aspects of explosive cyclones in the Mediterranean, *Int. J. Climatol.*, 31, 1785–1802,
768 <https://doi.org/10.1002/joc.2203>.
769

770 Latha, P. T., Rao, K.H., Nagamani, P.V., Amminedu, E., Choudhury, S.B., Dutt, C.B.S. and Dadhwal,
771 V.K., 2015. Impact of Cyclone PHAILIN on Chlorophyll-a Concentration and Productivity in the Bay
772 of Bengal. *International Journal of Geosciences*, 6, 473-480, doi: [10.4236/ijg.2015.65037](https://doi.org/10.4236/ijg.2015.65037).
773

774 Law K., 2011. The Impact of Oceanic Heat Content on the Rapid Intensification of Atlantic Hurricanes,
775 Chapter 17. In: Lupo, A., eds. *Recent Hurricane Research - Climate, Dynamics, and Societal Impacts*.
776 Croatia : InTech: 331-354.
777

778 Li, D., Chang, P., Ramachandran, S., Jing, Z., Zhang, Q., Kurian, J., Gopal, A., & Yang, H. (2021).
779 Contribution of the Two Types of Ekman Pumping Induced Eddy Heat Flux to the Total Vertical Eddy

780 Heat Flux. *Geophysical Research Letters*, 48(9), e2021GL092982.
781 <https://doi.org/10.1029/2021GL092982>.
782
783 Lin, I. I., Goni, G. J., Knaff, J. A., ZForebas, C., Ali, M. M.,2013. Ocean heat content for tropical
784 cyclone intensity forecasting and its impact on storm surge, *Nat. Hazards*, 66, pp. 1481-1500,
785 10.1007/s11069-012-0214-5
786
787 Liu, Y., Tang, D., Tang, S., Morozov, E., Liang, W., Sui, Y.,2020. A case study of Chlorophyll a
788 response to tropical cyclone Wind Pump considering Kuroshio invasion and air-sea heat exchange.
789 *Science of Total Environment*, 741:140290. doi: 10.1016/j.scitotenv.2020.140290. Epub 2020 Jun 18.
790 PMID: 32603939.
791
792 Ma, Z.,2018. Examining the contribution of surface sensible heat flux induced sensible heating to
793 tropical cyclone intensification from the balance dynamics theory. *Dynamics of Atmospheres and*
794 *Oceans*, 84, 33–45. <https://doi.org/10.1016/j.dynatmoce.2018.09.001>
795
796 MedECC.,2020. Climate and environmental change in the Mediterranean Basin—Current situation and
797 risks for the future. In W. Cramer, J. Guiot, & K. Marini (Eds.), *First Mediterranean assessment report*,
798 Union for the Mediterranean, Plan Bleu (p. 632). UNEP/MAP.
799
800 Menna, M., Martellucci, R., Reale, M. *et al.*,2023 A case study of impacts of an extreme weather system
801 on the Mediterranean Sea circulation features: Medicane Apollo (2021). *Scientific Report*, 13, 3870, doi:
802 [10.1038/s41598-023-29942-w](https://doi.org/10.1038/s41598-023-29942-w).
803
804 Miglietta, M.M.,Rotunno, R., 2019. Development Mechanisms for Mediterranean Tropical-like
805 Cyclones (Medicanes). *Q. J. R. Meteorol. Soc.* 145, 1444–1460.
806
807 Mishra, A.K., Jangir, B. & Strobach, E., 2024. Influence of mesoscale sea-surface temperature
808 structures on the Mediterranean cyclone Ianos in convection-permitting simulations: Contributions of
809 surface warming and cold wakes. *Quarterly Journal of the Royal Meteorological Society*, 150(765),
810 5146–5166. <https://doi.org/10.1002/qj.4862>
811
812 Morrow, R., et al.,2019. "Global observations of fine-scale ocean surface topography with the Surface
813 Water and Ocean Topography (SWOT) mission." *Frontiers in Marine Science*, 6, 232.
814 <https://doi.org/10.3389/fmars.2019.00232>.
815
816 Nicolaides, K. A., Michalelides, S. C., and Karacostas, T. (2006). Synoptic and dynamic characteristics
817 of selected deep depressions over Cyprus, *Adv. Geosci.*, 7, 175–180, [https://doi.org/10.5194/adgeo-7-](https://doi.org/10.5194/adgeo-7-175-2006)
818 [175-2006](https://doi.org/10.5194/adgeo-7-175-2006), 2006.
819
820 Normand, J.C.L., Heggy, E., 2024. Assessing flash flood erosion following storm Daniel in Libya. *Nat*
821 *Commun* 15, 6493. <https://doi.org/10.1038/s41467-024-49699-8>
822
823 Oliver, E.C.J., Donat, M.G., Burrows, M.T. *et al.*, 2018. Longer and more frequent marine heatwaves
824 over the past century. *Nat Commun* 9, 1324. <https://doi.org/10.1038/s41467-018-03732-9>
825

826 Panegrossi, G., D'Adderio, L. P., Dafis, S., Rysman, J.-F., Casella, D., Dietrich, S., & Sanò, P., 2023.
827 Warm Core and Deep Convection in Medicanes: A Passive Microwave-Based Investigation. *Remote*
828 *Sensing*, 15(11), 2838. <https://doi.org/10.3390/rs15112838>
829

830 Pytharoulis, I., Kartsios, S., Tegoulas, I., Feidas, H., Miglietta, M. M., Matsangouras, I., & Karacostas,
831 T.,2018. Sensitivity of a Mediterranean Tropical-Like Cyclone to Physical Parameterizations.
832 *Atmosphere*, 9(11), 436. <https://doi.org/10.3390/atmos9110436>
833

834 Raveh-Rubin, S. and Flaounas, E., 2017. A dynamical link between deep Atlantic extratropical cyclones
835 and intense Mediterranean cyclones. *Atmospheric Science Letters*, 18: 215-221.
836 <https://doi.org/10.1002/asl.745>
837

838 Reale, M., Cabos, W., Cavicchia, L., Conte, D., Coppola, E., Flaounas, E., et al.,2022. Future
839 projections of Mediterranean cyclone characteristics using the Med-CORDEX ensemble of coupled
840 regional climate system models. *Climate Dynamics*, 58(9–10), 2501–2524.
841 <https://doi.org/10.1007/s00382-021-06018-x>
842

843 Reynolds, R. W., Smith, T. M., Liu, C., Chelton, D. B., Casey, K. S., and Schlax, M. G., 2007. Daily
844 High-Resolution-Blended Analyses for Sea Surface Temperature. *J. Climate*, 20, 5473–5496,
845 <https://doi.org/10.1175/2007JCLI1824.1>.
846

847 Scardino, G., Kushabaha, A., Miglietta, M. M., Bonaldo, D., and Scicchitano, G.: When storms stir the
848 Mediterranean depths: chlorophyll *a* response to Mediterranean cyclones, *Ocean Sci.*, 21, 2849–2872,
849 <https://doi.org/10.5194/os-21-2849-2025>, 2025.
850

851 Scardino, G., Miglietta, M.M., Kushabaha, A. *et al.*,2024. Fingerprinting Mediterranean hurricanes
852 using pre-event thermal drops in seawater temperature. *Sci Rep* 14, 8014.
853 <https://doi.org/10.1038/s41598-024-58335-w>
854

855 Shang, X.-D., Zhu, H.-B., Chen, G.-Y., Xu, C., & Yang, Q.,2015. Research on cold core eddy change
856 and phytoplankton bloom induced by typhoons: Case studies in the South China Sea. *Advances in*
857 *Meteorology*, 1–19.doi: [10.1155/2015/340432](https://doi.org/10.1155/2015/340432).
858

859 Shang, X.-D., Zhu, H.-B., Chen, G.-Y., Xu, C., & Yang, Q.,2015. Research on cold core eddy change
860 and phytoplankton bloom induced by typhoons: Case studies in the South China Sea. *Advances in*
861 *Meteorology*, 1–19.doi: [10.1155/2015/340432](https://doi.org/10.1155/2015/340432).
862

863 Sharma, V., & Ali, M. M.,2014. Importance of ocean heat content for cyclone studies. *Journal of*
864 *Climatology & Weather Forecasting*, 2(1), 1–6. [https://www.longdom.org/open-access/importance-of-](https://www.longdom.org/open-access/importance-of-ocean-heat-content-for-cyclone-studies-9577.html)
865 [ocean-heat-content-for-cyclone-studies-9577.html](https://www.longdom.org/open-access/importance-of-ocean-heat-content-for-cyclone-studies-9577.html)
866

867 Strobach, E., Mishra, A.K., Jangir, B. *et al.*, 2024. Intensification of a rain system imparted by
868 Mediterranean mesoscale eddies. *Sci Rep* 14, 26810. <https://doi.org/10.1038/s41598-024-76767-2>
869

870 Stern, M., 1965, Interaction of a uniform wind stress with a geostrophic vortex, *Deep Sea Res. Oceanogr.*
871 *Abstr.*, 12(3), 355–367.
872

873 Sun, M., Tian, F., Liu, Y., & Chen, G., 2017. An Improved Automatic Algorithm for Global Eddy
874 Tracking Using Satellite Altimeter Data. *Remote Sensing*, 9(3), 206. <https://doi.org/10.3390/rs9030206>
875

876 Trigo, I. F., Bigg, G. R., and Davies, T. D., 2002. Climatology of cyclogenesis mechanisms in the
877 Mediterranean, *Mon. Weather Rev.*, 130, 549–569.
878

879 Vidya, P. J., Balaji, M., Mani Murali, R., 2021. Cyclone Hudhud-eddy induced phytoplankton bloom
880 in the northern Bay of Bengal using a coupled model, *Progress in Oceanography*, Volume 197, 102631,
881 ISSN 0079-6611, <https://doi.org/10.1016/j.pocean.2021.102631>.
882

883 Volpe, G., Buongiorno Nardelli, B., Colella, S., Pisano, A. and Santoleri, R.,2018. An Operational
884 Interpolated Ocean Colour Product in the Mediterranean Sea, in *New Frontiers in Operational*
885 *Oceanography*, edited by E. P. Chassignet, A. Pascual, J. Tintorè, and J. Verron, pp. 227–244.
886

887 Volpe, G., Colella, S., Brando, V. E., Forneris, V., Padula, F. L., Cicco, A. D., & Santoleri, R.,2019.
888 Mediterranean Ocean Colour Level 3 operational multi-sensor processing. *Ocean Science*, 15(1), 127-
889 146.
890

891 Wada, A., & Usui, N.,2007. Impact of tropical cyclone heat potential on tropical cyclone intensity in
892 the western North Pacific Ocean. *Journal of Oceanography*, 63(3), 505–516.
893 <https://doi.org/10.1007/s10872-007-0039-0>
894

895 Wada, A., Usui, N., 2007. Importance of tropical cyclone heat potential for tropical cyclone intensity
896 and intensification in the Western North Pacific. *J Oceanogr* 63, 427–447.
897 <https://doi.org/10.1007/s10872-007-0039-0>
898

899 Tranchant, Y. T., Legresy, B., Foppert, A., et al., 2025. SWOT reveals fine-scale balanced motions and
900 dispersion properties in the Antarctic Circumpolar Current. *ESS Open Archive* .
901 [10.22541/essoar.173655552.25945463/v1](https://doi.org/10.22541/essoar.173655552.25945463/v1)
902

903 Zhang, Z., & Qiu, B.,2020. Surface Chlorophyll Enhancement in Mesoscale Eddies by Submesoscale
904 Spiral Bands. *Geophysical Research Letters*, 47, e2020GL088820.
905 <https://doi.org/10.1029/2020GL088820>
906

907 Zhao et al., 2019. A MATLAB toolbox to detect and analyze marine heatwaves. *Journal of Open Source*
908 *Software*, 4(33), 1124, <https://doi.org/10.21105/joss.01124>
909

910 Zittis, G., Almazroui, M., Alpert, P., Ciais, P., Cramer, W., Dahdal, Y., et al.,2022. Climate change and
911 weather extremes in the Eastern Mediterranean and Middle East. *Reviews of Geophysics*, 60(3),
912 e2021RG000762. <https://doi.org/10.1029/2021RG000762>.
913
914
915